ADVANCED PHYSICS RESEARCH Open Access
www.advphysicsres.com

Anatomy of the Dynamics of the Nucleation of Skyrmions in Nanodots via the Voltage-Controlled Magnetic Anisotropy

Pablo Olleros-Rodríguez, Adrián Gudín, Julio Camarero, Oksana Chubykalo-Fesenko,* and Paolo Perna**

Electric fields can be employed to efficiently manipulate spin textures in low-dimensional magnetic systems. In this work, the field-free formation of magnetic skyrmions in ferromagnetic-based patterned nanodots with perpendicular magnetic anisotropy and Dzyaloshinskii–Moriya interaction via the voltage-controlled magnetic anisotropy is studied. By micromagnetic simulations it is demonstrated that by reducing the magnetic anisotropy via an electric voltage pulse with adequate intensity and raise and decay times, it is possible to achieve 100% skyrmion nucleation probability through an intermediate magnetic vortex. The nucleation path is investigated in a Graphene/Co/Pt nanodot varying Co thickness, temperature, and applied field. A complete nucleation/annihilation process via bipolar voltage pulses is also possible enabling the realization of a writing/deleting logic device. The results reveal the relevance of following a quasi-equilibrium magnetization dynamical path and elucidates the relevance of the absolute stability of the magnetic skyrmion state against other possible magnetic configurations.

1. Introduction

Magnetic skyrmions[1,2] are nanometer-size chiral spin textures that hold promise for next-generation electronics, novel architectures for in-memory processing, neuromorphic- and reservoir-computing.[3–6] The benefits of skyrmions arise from their specific stable topologically non-trivial magnetic configuration that can be secured by the interplay of different energetic contributions.[7] Among them, perpendicular magnetic anisotropy (PMA) confers to magnetic skyrmions a large stability against thermal fluctuations, whereas Dzyaloshinskii–Moriya interaction (DMI) induces the chiral character. Both contributions originate from the spin-orbit coupling (SOC)[8] due to the orbital hybridization and the breaking of the spatial symmetry at the interfaces.[9,10] Besides, the special closed-shape configuration of skyrmions determine their topological protection,[8,11–13] conferring robustness against magnetic field and/or defects. This is due to the fact that the evolution of a magnetic skyrmion toward other magnetic configurations is energetically not favorable. The stability of the nucleated skyrmions and the minimum energy paths (energy barriers) leading to their collapse, both in continuous and confined systems, and considering pinning due to material defects, have been explored elsewhere.[14–17]

The successful development of skyrmionic devices requires the engineering of heterostructures whose properties are designed to ensure easy nucleation and stabilization of skyrmions.[7,18–20] The nucleation of skyrmions is usually achieved by employing external magnetic fields, electric currents, short or ultra-short light pulses, or by exploiting geometrical constraints.[21–24] However, the drawbacks of these methods lie in possible overheating, complexity of miniaturization or lack of scalability. In the contrary, the ability to control the magnetic properties through the application of electric fields represents a significant advantage in terms of energy consumption, processing speed and architectural design. For these reasons, the interest on the electric-field-induced manipulation of magnetism has experienced a boost in the last decade within the scientific community.[25–28] This is mostly due to the advances obtained in the preparation of heterostructures combining materials with different properties, as magnetoelectric (ME), piezoelectric, ferroelectric, multiferroic, or even 2D materials.[29–32]

P. Olleros-Rodríguez[+], A. Gudín, J. Camarero, P. Perna
IMDEA Nanoscience, C/ Faraday 9, Campus de Cantoblanco
Madrid 28049, Spain
E-mail: pablo.olleros@imdea.org; paolo.perna@imdea.org
A. Gudín, J. Camarero
Departamento de Física de la Materia Condensada
Instituto Nicolás Cabrera and Condensed Matter Physics Center (IFIMAC)
Universidad Autónoma de Madrid, Campus de Cantoblanco
Madrid 28049, Spain
J. Camarero, O. Chubykalo-Fesenko, P. Perna
Unidad de Nanomateriales Avanzados
IMDEA Nanociencia, Unidad asociada al CSIC
Madrid 28049, Spain
E-mail: oksana@icmm.csic.es
O. Chubykalo-Fesenko
Materials Science Institute of Madrid (ICMM-CSIC)
Campus de Cantoblanco
Madrid 28049, Spain

The ORCID identification number(s) for the author(s) of this article can be found under https://doi.org/10.1002/apxr.202400107

[+]Present address: Quantitative Methods Department, CUNEF Universidad, C/ Leonardo Prieto Castro, 2, Madrid 28040, Spain

DOI: 10.1002/apxr.202400107

In general, by subjecting a magnetic system to an external electric field it is possible to modify its magnetic properties as saturation magnetization, intra- and inter-layer exchange coupling, magnetic damping, etc.[28] However, a detailed and accurate description of the whole set of mechanisms lying behind ME effects is far from being completed. Different experimental and theoretical works report a linear variation of PMA and DMI by using electric field-induced ion migration, orbital modification, and magnetostriction.[33–36] Other works report on the use of electric fields to nucleate, stabilize and manipulate magnetic skyrmions,[37–41] with the added benefits of an easy implementation of scalable and low-energy-consuming magneto-electric devices.

In the present work, by micromagnetic simulations, we investigate the magnetization dynamics during the nucleation of magnetic skyrmions in magnetic nanodots via field-free voltage-controlled magnetic anisotropy (VCMA). Our simulations highlight the relevance of following a close-to-equilibrium magnetization dynamical path for the nucleation of a stable magnetic skyrmion achieved through an intermediate magnetic vortex state. The skyrmion nucleation path is investigated as a function of the system's parameters and of the protocol used (voltage raise and drop-off time). Skyrmion annihilation is also obtained demonstrating the possibility to realize reversible writing/deleting processes.

2. Results and Discussion

We have studied the dynamics of the nucleation of magnetic skyrmions in nanodots under the application of an external electric field in epitaxial Graphene (Gr)/ferromagnetic system that shows enhanced PMA and sizebale DMI, both of interfacial origin[32,42,43] and tunable by orbital hybridization.[44] In this system it has been previously demonstrated that magnetic skyrmions with a mixed Bloch–Néel chirality can be stabilized aided by the geometrical confinement imposed by the borders of the dot.[45]

Here, we focus on Gr/Co/Pt with Co thicknesses of $t_{Co} = 18$, 19, 20, and 21 monolayers (ML), i.e., close to the spin reorientation transition from perpendicular to in-plane magnetic anisotropy, to maximize the efficiency of the magnetic domain nucleation process.[40] Besides, we exploit the geometrical confinement in patterned nanodots with a diameter of 256 nm to stabilize isolated small magnetic skyrmions.[45] In fact, in previous studies we demonstrated that magnetic skyrmions are stabilized due to the confinement imposed by the border of the dot in the same multilayered structure[45–47] or by the direct interaction with other coexisting skyrmions in a skyrmion lattice.[24]

For the application of an electric voltage, we exploit a ferroelectric layer of Zr-doped HfO_x grown on top of the Gr/Co that provides high electrical polarization.[32] The sketch of the structure and the geometry for the application of the electric voltage is depicted in **Figure 1a**.

Our protocol for the nucleation of skyrmions under applied electric field is based on the electric-field-induced modification of the energetic landscape in nanosecond timescale dividing the ferromagnetic and the skyrmionic state. During this time the micromagnetic parameters (such as anisotropy) are changing the way the energy barrier becomes zero and the system dynamically goes to the new state. This is different from the evaluation of the reversal path via the energy barriers, e.g., using the nudged elastic band method[14–16,38,48] which searches for the saddle point in the energy landscape, maintaining the micromagnetic parameters constant.

The considered nucleation protocol (illustrated in Figure 1b) consists of an initial state which is relaxed from a saturated magnetic state having its magnetization pointing upward along the OOP direction. We assume that due to the effect of the electric field, the anisotropy of the system is reduced toward a stable value K_U^*. Following the reduction of the anisotropy, the system evolves toward an intermediate magnetic vortex. When the electric field is removed, the anisotropy of the system is recovered and a final magnetic skyrmion is nucleated.

For a given set of magnetic properties (including the thickness-dependent PMA with interfacial origin) the probability to obtain the intermediate vortex and the final skyrmion are studied based on the anisotropy reduction (K_U^*/K_U^0) and the rising (Δt_{rise}) and falling (Δt_{fall}) times of the applied external voltage pulse. For the given shape of the temporal profile of the electric field $E(t)$ seen in Figure 1c the reduction of the magnetic anisotropy is given by $K_{\text{eff}}(E(t); t_{Co}) = K_{\text{eff}}(E = 0; t_{Co}) + \frac{\beta_{\text{PMA}}}{t_{Co}} E(t)$. Here, the experimentally accessible parameter β_{PMA} defines the modification of the magnetic anisotropy energy in terms of the applied electric field. A detailed description of the computational method is presented in the Micromagnetic model section.

Simulations carried out at $T = 0$ K reveal that for sufficiently long rising and falling voltage times, the system evolves from the initial relaxed states toward an intermediate magnetic vortex having its core pointing parallel to the initial magnetization (called here parallel-vortex or P-Vortex state). From this intermediate P-vortex state, and considering the most adiabatic path in which the system is allowed to stabilize following slow variations of the anisotropy, a final magnetic skyrmion arises. In this adiabatic process, the system always shows axisymmetric magnetic configurations that are the most stable configurations at given reduced anisotropy (energetic study in Section S5, Supporting Information).

In order to reach the intermediate P-vortex state the topological charge acquires the value $Q = 0.5$ (orange region in **Figure 2a**). The latter feature allows to identify for each dot thickness the minimum reduction of the anisotropy $(K_U^*/K_U^0)_{min}$ necessary for reaching the intermediate P-Vortex state. We note that Q can assume values even larger than 0.5. This is due to the spins placed at the border of the dot that are canted with an OOP component with an opposite sign to that of the core of the vortex. Thus, at $(K_U^*/K_U^0)_{min}$, the time-inversion symmetry is broken and if the anisotropy of the system is recovered the system never evolves toward the initial relaxed state. We can observe that the required reduction of the anisotropy for obtaining the intermediate vortex state is lower for thicker dots (e.g., $(K_U^*/K_U^0)_{min} \simeq 0.87$ for $t_{Co} =$ 21 ML and $(K_U^*/K_U^0)_{min} \simeq 0.83$ for $t_{Co} = 18$ ML). This is due to the proximity to the spin-reorientation-transition which is thickness-dependent. As we are interested in the qualitative description of the nucleation path from now on we present the results corresponding to a 30% reduction of the anisotropy of the system under the effect of a constant electric field (i.e., $K_U^*/K_U^0 = 0.7$).

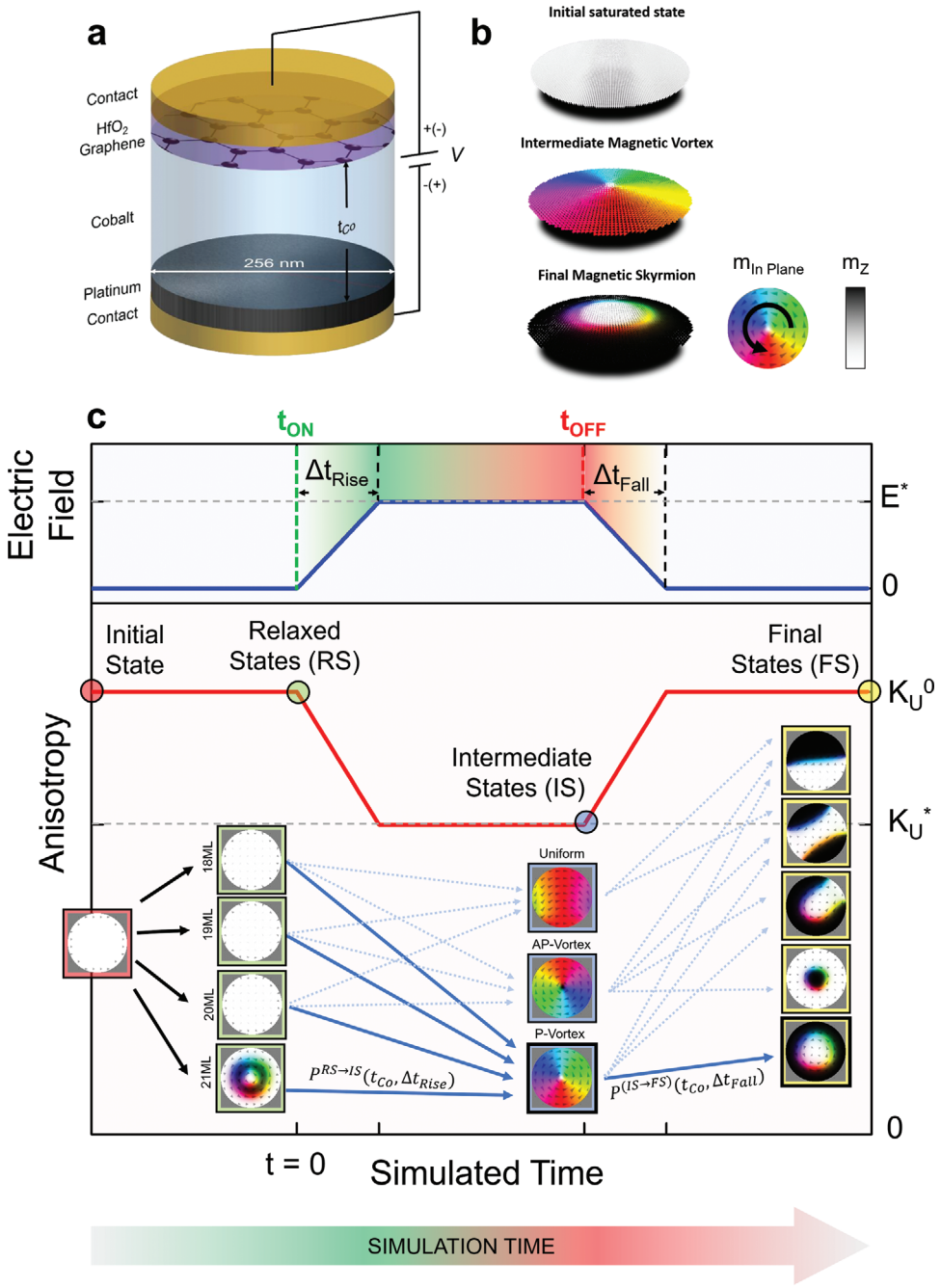

Figure 1. Overview of the nucleation process under the effect of an electric field a) Scheme of the multilayer structure for VCMA and functioning configuration. b) Zoom of magnetic configurations in (c). c) The electric field (blue line) is defined by its rising Δt_{rise} and falling Δt_{fall} times. The effect of the electric field is introduced as a proportional response of the effective anisotropy of the system (red line) reaching a value $K^*_{eff} = 0.7K^0_{eff}$. The nucleation protocol consists of an initial saturated state (top configuration in b) that evolves toward an intermediate vortex state (middle in b) and then toward a final magnetic skyrmions (bottom in b).

In the following, we study first the probability of reaching the intermediate P-Vortex state from the initial relaxed state and then from this intermediate P-Vortex state toward the final magnetic skyrmion at room temperature (i.e. $T = 300$ K).

We start with a nanodot having its magnetization oriented upward along the OOP direction (white magnetic dot in bottom-left box in Figure 1). The initial relaxed state is obtained by integrating the stochastic Landau–Lifshitz–Gilbert (LLG) equation at a given temperature during 5 ns. Depending on the Co thickness, this initial state may be a saturated or a quasi-vortex state.[45] (see relaxed states (RS) in Figure 1c).

The electric voltage pulse with a rising time of Δt_{rise} is then applied in the structure along the OOP direction and the anisotropy drop drives the magnetic configuration to in plane. At this point

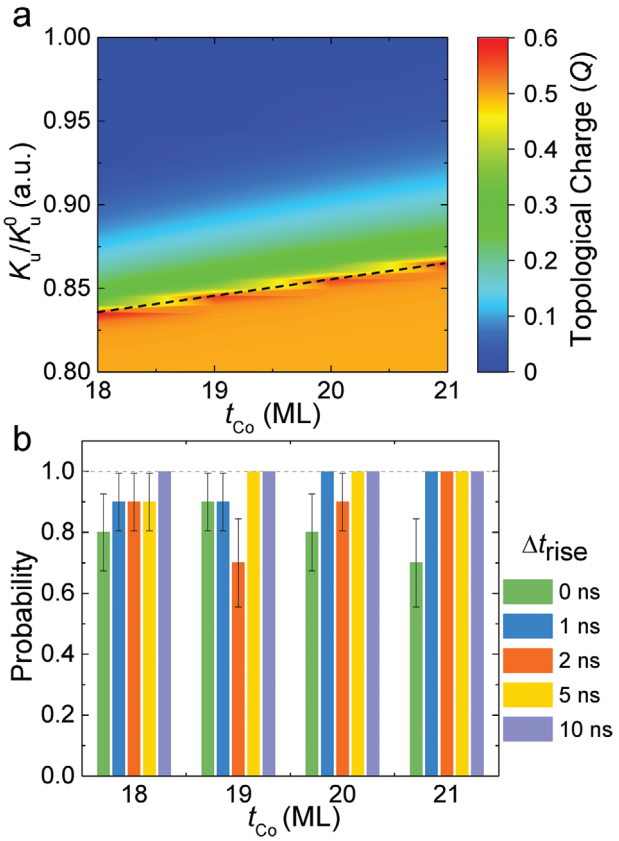

Figure 2. Voltage-induced nucleation of intermediate magnetic vortex a) Topological charge of the most stable state depending on the reduction of the anisotropy K_U/K_U^0 and on t_{Co}. The dashed line represents the critical reduction of the anisotropy at which the system is not able to return to the initial saturated state. b) Transition probability toward the intermediate P-vortex state as function of t_{Co} and Δt_{rise}.

(i.e., $K_U = K_U^*$) we found that in the presence of thermal fluctuations the system can show three different magnetic states, namely uniform, vortex with the core antiparallel to the initial state (AP-Vortex) and vortex with the core parallel to the initial state (P-Vortex) (see Intermediate States in Figure 1c). In Figure 2b we show the probabilities of obtaining an intermediate P-Vortex state from the initial saturated state for $\Delta t_{rise} = 0$, 1, 2, 5, and 10 ns upon a 30% reduction of the anisotropy. Due to the stochastic nature of thermal fluctuations, these results were averaged over ten different sets of simulations. We can clearly observe that in all cases, the 100% nucleation probability is obtained for the longest pulse ($\Delta t_{rise} = 10$ ns; purple bars). As described previously, by reducing slowly the anisotropy of the system, the magnetization tends to go in-plane displaying an axisymmetric configuration during the transition. On the contrary, if the anisotropy is reduced too fast, more vortices might be nucleated in the dot resulting in complex magnetization dynamics including (anti)vortex-(anti)vortex interactions and (anti)vortices gyrotropic motion which can cause the appearance of AP-Vortex and quasi-uniform states (illustrated in the bottom panel boxes in Figure 1c).

Starting from the intermediate P-Vortex state, which has been stabilized at the reduced anisotropy $K_U^*(t_{Co}) = 0.7K_U^0(t_{Co})$, we then study the transition toward the final states. To do so, the electrical voltage is removed during different falling times $\Delta t_{fall} = 0$, 1, 2, 5, 10, and 20 ns, and the anisotropy recovers linearly to the initial value.

Through a careful inspection of the magnetization dynamics during this process, we can identify two dynamical stages. At first, the recovery of the OOP orientation of the spins takes place at the core of the dot and border. As this stage starts from a P-vortex state, in the center of the dot a magnetic domain pointing parallel to the initial magnetization is expanded outward. At the same time, spins placed at the border of the dot start to realign pointing most of them antiparallel to the domain at the core. However, due to thermal fluctuations some of the spins placed at the border may flip pointing parallel to the core domain. Thus we found that the system can evolve showing an axisymmetric (that is, the most stable) or a non-axisymmetric magnetic configuration (**Figure 3**). In both cases, during the spin-reorientation, the magnetization dynamics consists in the outward expansion of the core domain and the inward expansion along the radial direction of parallel or antiparallel magnetic domains starting from the border.

Once the expansion of the OOP magnetic domain has taken place spin-up and spin-down magnetic domains will meet and a magnetic domain wall (DW) appears. During the second dynamic stage the DW changes its shape and curvature so that the magnetic magnetic domains placed at the border can be expanded not only in the radial direction but also creep along the border. If the system follows the axially-symmetric path during the first dynamic stage, then the final state is a P-skyrmion. However, P-skyrmion can be also obtained from a non-axisymmetric configuration through the expansion, during the DW dynamics stage, of the antiparallel magnetic domain along the border of the dot.

In the situation in which the system shows a non-axisymmetric magnetic configuration during the spin-reorientation and it is not able to transit to a closed structure during the DW dynamics the system reaches a final stripe domain (SD) state. Here, the final curvature of the DW separating spin-up and spin-down states is dependent on the thickness of the dot. We can classify three resulting SD configurations: straight DW for $t_{Co} = 18$, 19 ML, horse-shoe shaped DW for 20 ML, and skyrmion for 21 ML, as seen in Figure 3.

At room temperature (RT), the probability to nucleate P-skyrmions $\mathcal{P}^{(Sk)}$ as function of Δt_{fall} and t_{Co} is shown in **Figure 4a**. Once again, for adiabatic transitions computed at $T = 0$ K and for sufficiently large falling times of the voltage pulse Δ_{fall}, the system always shows an axisymmetric magnetic configuration leading toward a final magnetic skyrmion. However, due to thermal fluctuations at RT some spins placed at the border flip and are aligned pointing parallel to the core promoting the growth of the non-axisymmetric magnetic configurations. In these situations, the probability of nucleating magnetic skyrmions depends exclusively on the transition probability from non-axisymmetric toward the axisymmetric magnetic configuration.

The influence of temperature on the final results has been studied considering low temperatures (i.e., $T = 10$ K) and RT (i.e., $T = 300$ K) (see the detailed description in Sections S1 and S2, Supporting Information). The role of thermally activated transitions is highlighted through the energetic study of the final magnetic configurations (Figure 4b) that reveals that magnetic

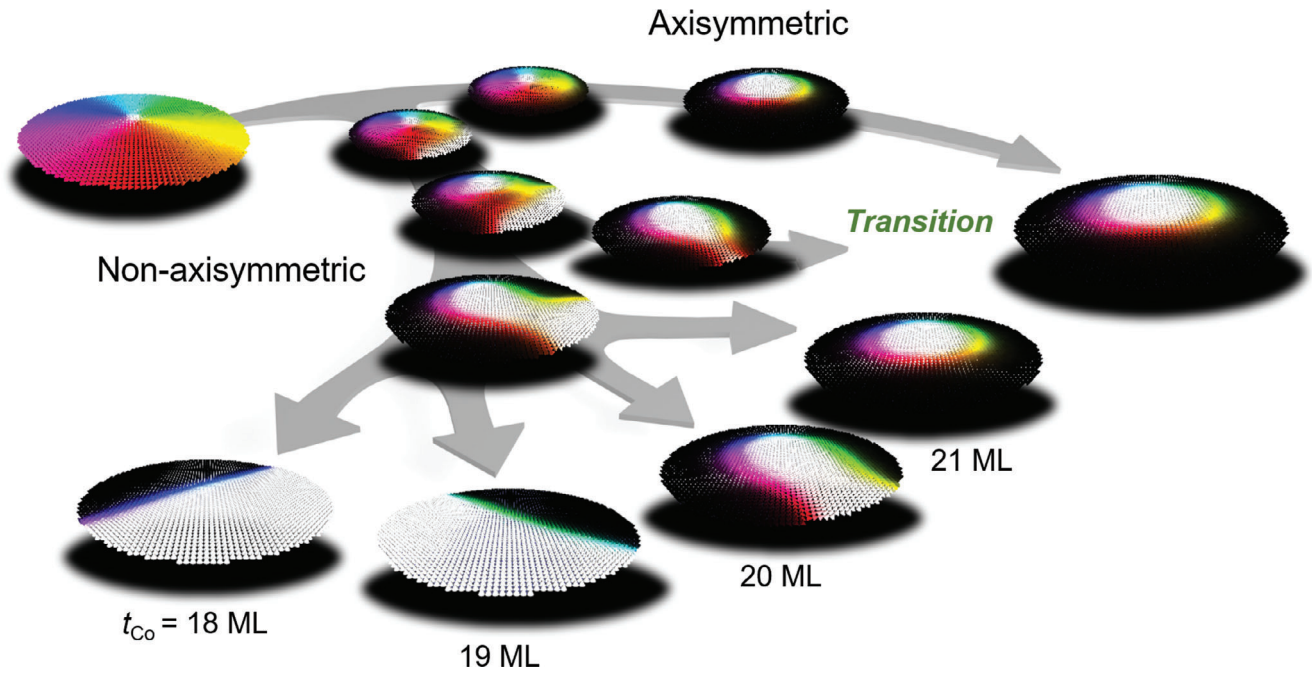

Figure 3. Anatomy of the dynamics of skyrmion nucleation. Possible transitions from the intermediate P-Vortex state (beige background) toward the final states (light green background) represented by stripe domains (SD) or skyrmions (Sk). During the transition, the system can follow a dynamical path represented by pure axisymmetric configurations (dark blue background) or non-axysimmetric configurations (light blue background). In the latter case, there is a certain probability to jump toward an axisymmetric configuration leading to a final skyrmionic state. Note that final SD states show domain walls with different curvature depending on the dot thickness (t_{Co}).

skyrmions are the most stable configuration of the system for thicknesses above $t_{Co} \geqslant 20$ ML. Thus, at RT, thermal fluctuations are large enough to overcome energy barriers dividing non-axisymmetric and axisymmetric configurations and, as a result, the system always reach the stable skyrmionic state.

For thinner dots (i.e., $t_{Co} < 20$ ML) we must remark that, although magnetic skyrmion is not the most stable state, during the recovery of the anisotropy, axisymmetric magnetic configurations are more stable than non-axisymmetric ones (energetic study in Section S5, Supporting Information). Thus, the nucleation probability increases for longer falling times of the voltage pulse Δt_{fall} as the system has more time to transit to an axisymmetric magnetic configuration during the recovery of the anisotropy. The fact that we have never observed an axisymmetric magnetic configuration being broken into a non- axisymmetric one allow us to infer that the energy barriers surrounding the axisymmetric configurations are large enough to impede thermally activated transitions toward a final SD state in all cases even at RT.

In summary, for sufficiently slow processes and low temperatures, the most probable path for the nucleation of skyrmions is an adiabatic (at $T = 0$ K) and quasi-adiabatic ($T > 0$ K) paths, corresponding to axisymmetric configurations. At $T = 300$ K, and for any t_{Co} the probability of the axisymmetric magnetic configurations its almost zero and the nucleation of P-skyrmion depends on thermally activated transitions to the most stable state (Figure S4, Supporting Information). At $T > 0$ K, the nucleation of P-Skyrmion is achieved either through a (axisymmetric) quasi-adiabatic path, or through a (non-axisymmetric) non-adiabatic path plus a thermally activated transition to a quasi-adiabatic regime.

Note that, although the application of an external voltage pulse modifies also the DMI of the system,[35,36] we have not observed any effect on the nucleation probabilities (Section S3, Supporting Information).

Our results were obtained considering epitaxial Zr-doped HfO_x / Gr/Co/Pt with high-quality interfaces[42] and low level of disorder. However, since the skyrmion formation is obtained from the domain walls dynamics, the existence of pinning centers, as defects, can modify the nucleation process.[49] Defects are introduced in our simulation by modulating the anisotropy through a normal distribution with different intensities and directions over the dot (see Micromagnetic Model Section). While for the cases of $t_{Co} = 18$, 19 ML the introduction of defects strongly reduces the nucleation probabilities, for the cases of thicker films (i.e., $t_{Co} \geqslant 20$ ML), since the skyrmionic state is more stable than the stripe domain state, the nucleation probability does not seem to be affected. However, it will take a longer time to overcome the pinning barrier and reach the skyrmionic state. See Section S6 (Supporting Information) for details.

Finally, we have studied the effect of the application of a weak external magnetic field of $B_{ext} = -5$ mT pointing antiparallel to the initial magnetization of the system (i.e., pointing downward). We observe that the external magnetic field favors the growth of the outer magnetic domain pointing antiparallel to the core of the dot. This leads the system toward an axisymmetric magnetization configuration so the nucleation of final P-Skyrmion is achieved for all Co thicknesses, temperatures and for $\Delta t_{fall} \geqslant 1$ ns. (The complete study of the nucleation process under the effect of the external field is presented in Section S4 Supporting Information). Moreover, the application of such external magnetic field

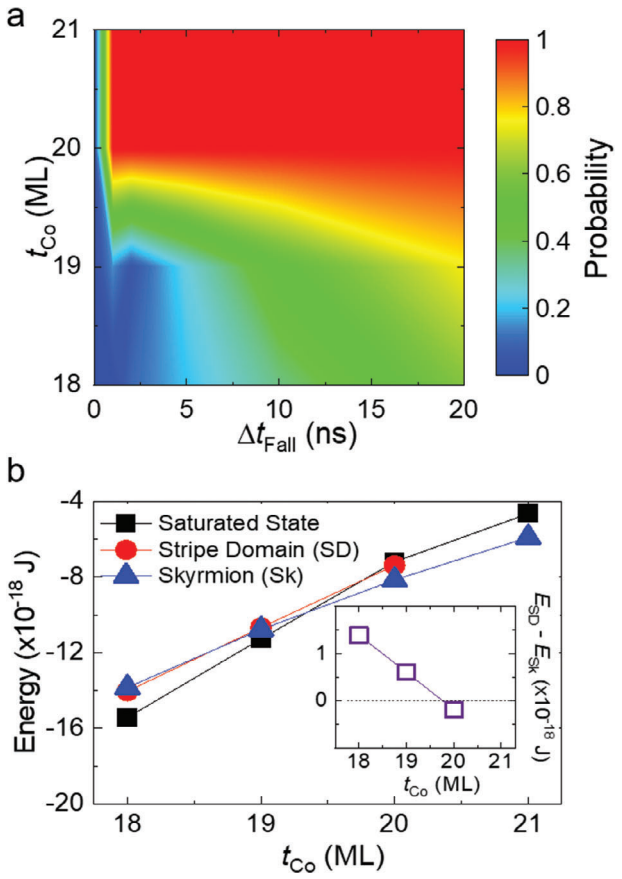

Figure 4. Voltage-induced nucleation of skyrmion a) Skyrmion nucleation probabilities at $T = 300$ K as function of t_{Co} and Δt_{Fall}. b) Energetic study of the final states in terms of the dot thickness t_{Co}. The energy of final magnetic configurations that can be reached after the application of the voltage pulse (Stripe domain red circles and Magnetic skyrmion blue triangles) are contrasted to that of the saturated states (black squares). The skyrmionic state becomes the most stable state for thicknesses above $t_{Co} \geqslant 20$ ML (See inset).

is enough to overcome the pinning, so that we always observe a final magnetic skyrmion at any considered thickness and in the presence of disorder.

We must note that although the presence of the external magnetic field modifies the energetic landscape of the system, the magnetic skyrmion state is not the most stable configuration for thicknesses below $t_{Co} < 20$ ML (Figure S8, Supporting Information). This result reveals that the 100% nucleation probability is achieved due to the promotion of the growth of the outer domain pointing antiparallel to the the core and not because the skyrmions are the most stable state of the system. Also, the presence of the external field does not prevent the system to reach the intermediate P-Vortex state (Figure S7, Supporting Information). On the contrary, the presence of the external field implies a smaller reduction of the anisotropy required to reach the vortex state. Besides, the topological charge does not show any modification induced by a reduction of DMI for any t_{Co} (Figure S6, Supporting Information). From a practical point of view, such a small external magnetic field can be incorporated into the system through a bias field layer[50] simplifying notably the architecture of the device.

Finally, we study the possibility of skyrmion annihilation via VCMA. In analogy to the voltage-driven anisotropy reduction employed during the nucleation process, we have simulated the effect of an anisotropy enhancement of 30% of its initial value due to an opposite external voltage pulse. As seen in **Figure 5**, while lowering anisotropy produces an increase in skyrmion diameter, an increase in anisotropy favors the reduction of the skyrmion diameter.[17] Therefore, the skyrmion reduces its size until its annihilation, and the final magnetic state of the dot is a uniform saturated magnetization with its vector pointing antiparallel to the initial state. Then, we can apply a second electric field pulse to reduce the anisotropy and nucleate a new skyrmion with the magnetization in the core now aligned in the opposite direction. In this way, we demonstrate the possibility to write and delete skyrmions with the desired chirality in nanodots.

3. Conclusion

In summary, we have investigated the dynamics of field-free nucleation of skyrmions in ferromagnetic-based patterned nanodots with PMA and DMI via VCMA. We have examined in detail the skyrmion nucleation probability and its dynamical paths as a function of anisotropy reduction and the characteristic rising and falling times of the voltage pulse. The study has been applied to the case of Gr/Co(t_{Co})/Pt structures in which the orbital hybridization affecting the magnetic interfacial interaction can be achieved by applying an external OOP electric field. It is important to note that the use of patterned nanodots, which have revealed themselves as suitable platforms to stabilize magnetic skyrmions due to the geometrical confinement, play a major role in the considered nucleation process due to its specific axial symmetry.

We find that the most probable dynamical path for the nucleation of a magnetic skyrmion is through an intermediate vortex state, which corresponds to an axisymmetric configuration. We observe that in adiabatic ($T = 0$ K) and quasi-adiabatic ($T = 10$ K) paths, the skyrmion nucleation probability is enhanced when considering sufficiently slow variations of the VCMA. At higher temperature ($T = 300$ K) we do not observe adiabatic transitions toward final magnetic states and the skyrmion nucleation is instead driven by thermally activated processes. In order to force the system to follow a quasi-adiabatic path, a small external magnetic field pointing antiparallel to the initial magnetization of the system can be employed. Finally, we also demonstrated the possibility to obtain a complete nucleation/annihilation process via bipolar voltage pulses, enabling the realization of a writing/deleting logic device.

Our results reveal the importance of close-to-equilibrium magnetization dynamic path and provide hence the conditions needed to efficiently nucleate and annihilate magnetic skyrmions in nanodots for their implementation in novel spintronics architectures for the next-generation electronics. Interestingly, our results also demonstrate the possibility of tuning specific set of dot thicknesses and voltage pulse duration in which the skyrmion nucleation probability is close to 50%. Such a result is of great interest for the design of devices with probabilistic computation capabilities.

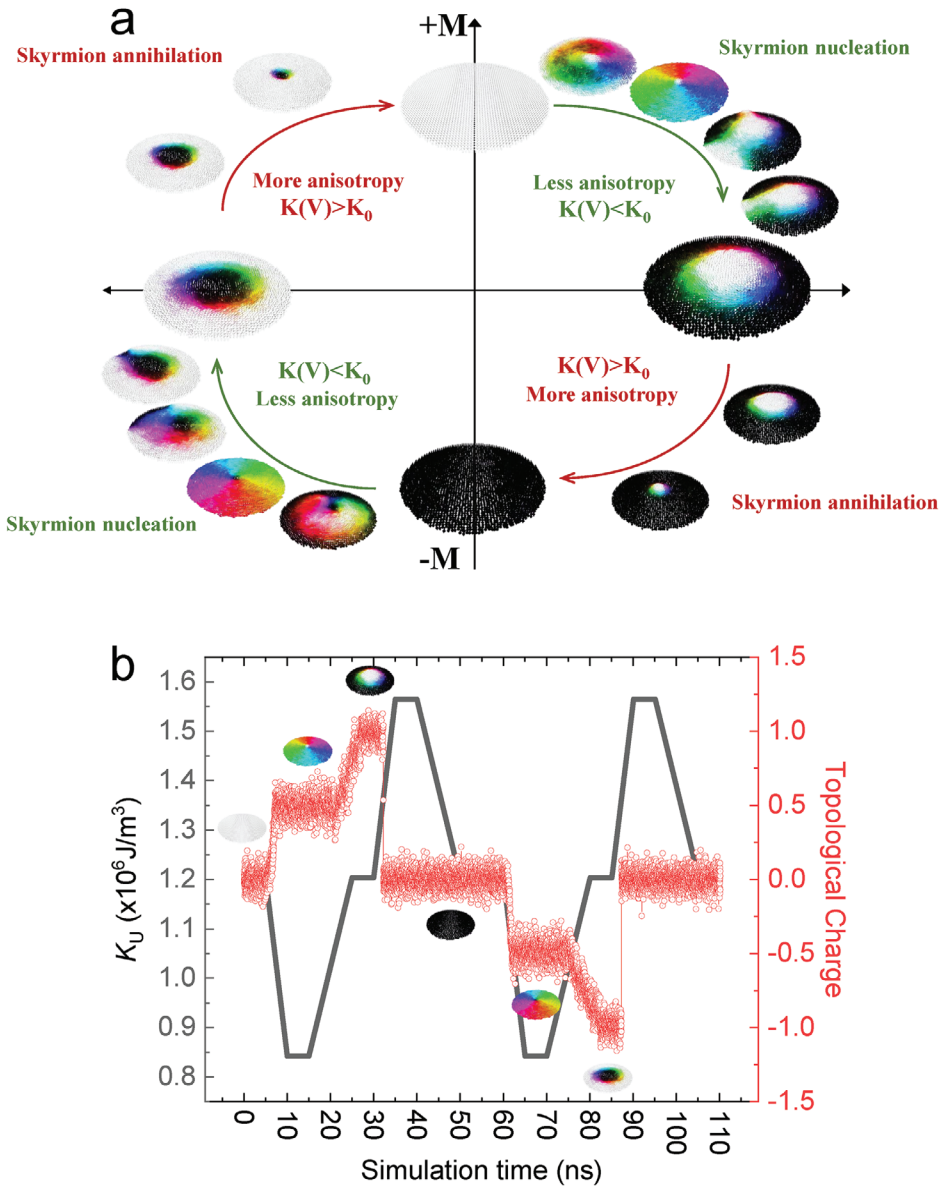

Figure 5. Writing/deleting skyrmion in dot by VCMA. From a saturated magnetization state (+M) (a) the skyrmion, with its core aligned to the initial magnetization, is nucleated through the application of a voltage pulse (positive) (b) that reduced the magnetic anisotropy of the dot. This process is achieved through the formation of an intermediate magnetic vortex state (as indicated in panel a). The skyrmion can be then annihilated by applying an opposite voltage pulse that increases the anisotropy of the dot and hence shrinks the skyrmion size. A final uniform state is obtained with opposite magnetization (–M). A second pulse will then reduce the anisotropy and nucleate a new skyrmion with the magnetization in the core now aligned in the opposite direction. The anisotropy and topological charge versus time is shown in panel b.

4. Micromagnetic Model

Micromagnetic simulations were carried out using the MuMax[3] computational code.[51,52] Dynamic studies were conducted by integrating the stochastic LLG equation:

$$\frac{\partial \vec{\mathbf{m}}}{\partial t} = \gamma_{\mathrm{LL}} \frac{1}{1+\alpha^2}\left(\vec{\mathbf{m}} \times \vec{\mathbf{B}}_{\mathrm{eff}} + \alpha(\vec{\mathbf{m}} \times (\vec{\mathbf{m}} \times \vec{\mathbf{B}}_{\mathrm{eff}}))\right) \quad (1)$$

in which the considered effective field contains the Zeeman ($\vec{\mathbf{B}}_{\mathrm{Zee}}$), magnetostatic ($\vec{\mathbf{B}}_{\mathrm{demag}}$), symmetric Heisenberg exchange ($\vec{\mathbf{B}}_{\mathrm{exch}}$), anisotropic ($\vec{\mathbf{B}}_{\mathrm{anis}}$), anti-symmetric Dzyaloshinskii-Moriya exchange ($\vec{\mathbf{B}}_{\mathrm{DMI}}$) and thermal ($\vec{\mathbf{B}}_{\mathrm{therm}}$):

$$\vec{\mathbf{B}}_{\mathrm{eff}} = \vec{\mathbf{B}}_{\mathrm{Zee}} + \vec{\mathbf{B}}_{\mathrm{demag}} + \vec{\mathbf{B}}_{\mathrm{exch}} + \vec{\mathbf{B}}_{\mathrm{anis}} + \vec{\mathbf{B}}_{\mathrm{DMI}} + \vec{\mathbf{B}}_{\mathrm{therm}} \quad (2)$$

Energetic studies were conducted by considering the minimization of the micromagnetic energy of the system being defined as:

$$\varepsilon = -\frac{1}{2} M_{\mathrm{Sat}} \vec{\mathbf{m}} \cdot \vec{\mathbf{B}}_{\mathrm{eff}} \quad (3)$$

were M_{Sat} is the saturation magnetization of the sample.

Following different theoretical and experimental reports, we consider a linear relationship of the effective magnetic anisotropy of the system K_{eff} with the electric field $E(t)$

$$K_{eff}(E(t);t_{Co}) = K_{eff}(E=0;t_{Co}) + \frac{\beta_{PMA}}{t_{Co}}E(t) \quad (4)$$

Where β_{PMA} is the so-called VCMA parameter and the effective anisotropy K_{eff} contains the information on the uniaxial anisotropy of the system K_u and the shape anisotropy $K_{shape} = \frac{1}{2}\mu_0 M_{Sat}^2$. Assuming that the electric field do not affect the magnetization saturation, the electric-field pulse $E(t)$ is introduced in the model by using the following expression for the implemented definition of the uniaxial anisotropy of the system:

$$K_u(E(t);t_{Co}) = K_u(E=0;t_{Co}) + \frac{\beta_{PMA}}{t_{Co}}E(t) \quad (5)$$

Where the thickness dependence is directly obtained by assuming the interfacial character of the PMA, thus:

$$K_u(E=0;t_{Co}) = \frac{K_S^{Gr/Co} + K_S^{Co/Pt}}{t_{Co}} + K_{Vol} \quad (6)$$

where $K_S^{Gr/Co}$ and $K_S^{Co/Pt}$ are the interfacial magnetic anisotropies of the Gr/Co and Co/Pt interfaces respectively, and K_{Vol} is the magnetic anisotropy of the cobalt volume.

It is worth noting that in this model it is possible to introduce an electric field affecting exclusively the Gr/Co (top) layer of the sample by assigning to the different regions of the sample the following definitions:

$$\begin{aligned} K_S^{Gr/Co}(E(t)) &= K_S^{Gr/Co}(E=0) + \beta_{PMA}E(t) \\ K_S^{Co/Pt}(E(t)) &= K_S^{Co/Pt}(E=0) \\ K_{Vol}(E(t)) &= K_{Vol}(E=0) \end{aligned} \quad (7)$$

Note that in the latter equations, the defined interfacial anisotropies are defined as surface energy densities, however, in the micromagnetic code the magnetic anisotropies are defined as volume energy densities. Both definitions are related by the thickness of a monolayer of cobalt which is chosen to be Δt_{Co} = 0.2 nm. As in the case of the effective magnetic anisotropy of the system, we introduce the effect of the voltage pulse in the model by considering a linear relationship of the Dzyaloshinskii–Moriya Interaction with the electric field

$$D_{eff}(E(t);t_{Co}) = D_{eff}(E=0;t_{Co}) + \beta_{DMI}E(t) \quad (8)$$

Note that given the dimensions of the effective DMI (surface energy density) the voltage-controlled effective DMI parameter β_{DMI} no longer needs to be divided by the cobalt thickness. Also, if we consider the interfacial character of the DMI

$$D_{eff} = (D_S^{Gr/Co} + D_S^{Co/Pt})\frac{\Delta t_{Co}}{t_{Co}} \quad (9)$$

Table 1. Table 1 Micromagnetic parameters used in the simulations.

Parameter	Value	Ref.
M_{Sat}	1.4 MA^{-1}	[45]
A_{exch}	24 pJ m^{-1}	[45]
α	0.3	[53]
$K_S^{Gr/Co}$ $(E=0)$	8.232 MJ m^{-3}	[45]
$K_S^{Co/Pt}$ $(E=0)$	2.743 MJ m^{-3}	[45]
K_{Vol}^{Co} $(E=0)$	0.728 MJ m^{-3}	[45]
$D_S^{Gr/Co}$ $(E=0)$	−1.41 mJ m^{-2}	[45]
$D_S^{Co/Pt}$ $(E=0)$	4.41 mJ m^{-2}	[45]

being Δt_{Co} = 0.2nm the thickness of a monolayer of cobalt, then it is possible to assign the effect of the electric field in the model by defining:

$$\begin{aligned} D_S^{Gr/Co}(E(t)) &= D_S^{Gr/Co}(E=0) + \frac{t_{Co}}{\Delta t_{Co}}\beta_{PMA}E(t) \\ D_S^{Co/Pt}(E(t)) &= D_S^{Co/Pt}(E=0) \end{aligned} \quad (10)$$

In **Table 1** we show the values used in the simulations for the magnetic anisotropies and the rest of the magnetic definitions.

The system has been modeled considering a $N_x \times N_y \times N_z$ = 128 × 128 × 1 mesh grid. The lateral sizes of each cell being $d_x = d_y$ = 2 nm and $d_z = t_{Co}$. When introducing temperature in micromagnetic simulations, thermal magnons with the capability to induce variations in the magnetic configurations have an associated decay length $\lambda_{ex,th} = \sqrt{\frac{A_{exch}}{\mu_0 M_S H_{th}}}$, with the thermal field $H_{th} = \sqrt{\frac{2\alpha k_B T}{\gamma \mu_0 M_S d_x d_y d_z \Delta t}}$.[54,55] Considering the micromagnetic parameters used in our simulations and assuming a time step Δt = 1×10 $^{-13}$ s, which is larger than the usual adaptative time step ($\Delta t_{adaptative} \leqslant 5 \times 10^{-14}$ s), the estimated thermal exchange length at RT (i.e., T = 300 K) is $\lambda_{ex,\,th}$ = 70.05 nm, which is almost two orders of magnitude larger than the unit cell size.

The disorder was introduced by defining 256 regions with different anisotropies. Particularly, the polar θ_U and azimuthal ϕ_U angles of the uniaxial anisotropy axis were defined randomly in between [0 $\leqslant\theta_U \leqslant$ 1°] and [0 $\leqslant\phi_U \leqslant$ 360°]. The intensity of the uniaxial anisotropy was obtained by multiplying the uniaxial anisotropy times a factor extracted from a normal random distribution centered in 1 and with σ = 0.025. This leads to a normal random distribution in which 98% of the regions have an anisotropy in between $0.95K_U^0$ and K_U^0.

Supporting Information

Supporting Information is available from the Wiley Online Library or from the author.

Acknowledgements

The authors acknowledge support from the Spanish AEI/MICINN Projects CNS2022-136143 (SPINCODE), PID2021-122980OB-C52 (ECLIPSE-ECoSOx), PCI2019-111867-2 (SOgraphMEM), PID2019-108075RB-C31,

CEX2020-001039-S, PID2020-116181RB-C3 (SOnanoBRAIN), and from the "(MAD2D-CM)-UAM" project funded by Comunidad de Madrid, by the Recovery, Transformation and Resilience Plan, and by, NextGenerationEU from the European Union. The authors acknowledge NVIDIA corporation for the donation of the Quadro P6000 used in the simulations.

Conflict of Interest

The authors declare no conflict of interest.

Data Availability Statement

The data that support the findings of this study are available from the corresponding author upon reasonable request.

Keywords

Dzyaloshinskii–Moriya interaction, electric field, graphene, skyrmions, voltage-controlled magnetic anisotropy

Received: July 18, 2024
Revised: October 7, 2024
Published online: November 28, 2024

[1] A. Fert, N. Reyren, V. Cros, *Nat. Rev. Mater.* **2017**, *2*, 1.
[2] G. Finocchio, F. Büttner, R. Tomasello, M. Carpentieri, M. Kläui, *J. Phys. D: Appl. Phys.* **2016**, *49*, 423001.
[3] K. M. Song, J.-S. Jeong, B. Pan, X. Zhang, J. Xia, S. Cha, T.-E. Park, K. Kim, S. Finizio, J. Raabe, J. Chang, Y. Zhou, W. Zhao, W. Kang, H. Ju, S. Woo, *Nat. Electron.* **2020**, *3*, 148.
[4] N. Sisodia, J. Pelloux-Prayer, L. D. Buda-Prejbeanu, L. Anghel, G. Gaudin, O. Boulle, *Phys. Rev. Appl.* **2022**, *18*, 014025.
[5] T. Yokouchi, S. Sugimoto, B. Rana, S. Seki, N. Ogawa, Y. Shiomi, S. Kasai, Y. Otani, *Sci. Adv.* **2022**, *8*, eabq5652.
[6] K. Raab, M. A. Brems, G. Beneke, T. Dohi, J. Rothörl, F. Kammerbauer, J. H. Mentink, M. Kläui, *Nat. Commun.* **2022**, *13*, 6982.
[7] F. Büttner, I. Lemesh, G. S. Beach, *Sci. Rep.* **2018**, *8*, 4464.
[8] A. Soumyanarayanan, N. Reyren, A. Fert, C. Panagopoulos, *Nature* **2016**, *539*, 509.
[9] S. Kim, S. Pathak, S. H. Rhim, J. Cha, S. Jekal, S. C. Hong, H. H. Lee, S.-H. Park, H.-K. Lee, J.-H. Park, S. Lee, H.-G. Steinrück, A. Mehta, S. X. Wang, J. Hong, *Adv. Sci.* **2022**, *9*, 2201749.
[10] D. Go, J.-P. Hanke, P. M. Buhl, F. Freimuth, G. Bihlmayer, H.-W. Lee, Y. Mokrousov, S. Blügel, *Sci. Rep.* **2017**, *7*, 1.
[11] R. Tomasello, K. Guslienko, M. Ricci, A. Giordano, J. Barker, M. Carpentieri, O. Chubykalo-Fesenko, G. Finocchio, *Phys. Rev. B* **2018**, *97*, 060402.
[12] D. Cortés-Ortuño, W. Wang, M. Beg, R. A. Pepper, M.-A. Bisotti, R. Carey, M. Vousden, T. Kluyver, O. Hovorka, H. Fangohr, *Sci. Rep.* **2017**, *7*, 4060.
[13] S.-G. Je, H.-S. Han, S. K. Kim, S. A. Montoya, W. Chao, I.-S. Hong, E. E. Fullerton, K.-S. Lee, K.-J. Lee, M.-Y. Im, J. Hong, *ACS nano* **2020**, *14*, 3251.
[14] D. Stosic, J. Mulkers, B. Van Waeyenberge, T. B. Ludermir, M. V. Milošević, *Phys. Rev. B* **2017**, *95*, 214418.
[15] D. Stosic, T. B. Ludermir, M. V. Milošević, *Phys. Rev. B* **2017**, *96*, 214403.
[16] P. F. Bessarab, G. P. Müller, I. S. Lobanov, F. N. Rybakov, N. S. Kiselev, H. Jónsson, V. M. Uzdin, S. Blügel, L. Bergqvist, A. Delin, *Sci. Rep.* **2018**, *8*, 3433.
[17] A. Aranda, A. Hierro-Rodriguez, G. Kakazei, O. Chubykalo-Fesenko, K. Guslienko, *J. Magn. Magn. Mater.* **2018**, *465*, 471.
[18] W. Legrand, D. Maccariello, F. Ajejas, S. Collin, A. Vecchiola, K. Bouzehouane, N. Reyren, V. Cros, A. Fert, *Nat. Mater.* **2020**, *19*, 34.
[19] S. Woo, K. Litzius, B. Krüger, M.-Y. Im, L. Caretta, K. Richter, M. Mann, A. Krone, R. M. Reeve, M. Weigand, P. Agrawal, I. Lemesh, M.-A. Mawass, P. Fischer, M. Kläui, G. S. D. Beach, *Nat. Mater.* **2016**, *15*, 501.
[20] C. Reichhardt, C. J. O. Reichhardt, M. Milošević, *Rev. Mod. Phys.* **2022**, *94*, 035005.
[21] J. Sampaio, V. Cros, S. Rohart, A. Thiaville, A. Fert, *Nat. Nanotechnol.* **2013**, *8*, 839.
[22] R. Juge, N. Sisodia, J. U. Larrañaga, Q. Zhang, V. T. Pham, K. G. Rana, B. Sarpi, N. Mille, S. Stanescu, R. Belkhou, M.-A. Mawass, N. Novakovic-Marinkovic, F. Kronast, M. Weigand, J. Gräfe, S. Wintz, S. Finizio, J. Raabe, L. Aballe, M. Foerster, M. Belmeguenai, L. D. Buda-Prejbeanu, J. Pelloux-Prayer, J. M. Shaw, O. Boulle, *Nat. Commun.* **2022**, *13*, 4807.
[23] W. Jiang, P. Upadhyaya, W. Zhang, G. Yu, M. B. Jungfleisch, F. Y. Fradin, J. E. Pearson, Y. Tserkovnyak, K. L. Wang, O. Heinonen, S. G. E. te Velthuis, A. Hoffmann, *Science* **2015**, *349*, 283.
[24] P. Olleros-Rodríguez, M. Strungaru, S. Ruta, P.-I. Gavriloaea, A. Gudín, P. Perna, R. Chantrell, O. Chubykalo-Fesenko, *Nanoscale* **2022**, *14*, 15701.
[25] S. Fusil, V. Garcia, A. Barthélémy, M. Bibes, *Annu. Rev. Mater. Res.* **2014**, *44*, 91.
[26] M. Weisheit, S. FÃhler, A. Marty, Y. Souche, C. Poinsignon, D. Givord, *Science* **2007**, *315*, 349.
[27] F. Matsukura, Y. Tokura, H. Ohno, *Nat. Nanotechnol.* **2015**, *10*, 209.
[28] C. Song, B. Cui, F. Li, X. Zhou, F. Pan, *Prog. Mater. Sci.* **2017**, *87*, 33.
[29] W. Eerenstein, N. Mathur, J. F. Scott, *nature* **2006**, *442*, 759.
[30] L. Herrera Diez, R. Kruk, K. Leistner, J. Sort, *APL Mater.* **2021**, *9*, 050401.
[31] A. Anadón, A. Gudín, R. Guerrero, I. Arnay, A. Guedeja-Marron, P. Jiménez-Cavero, J. M. Díez Toledano, F. Ajejas, M. Varela, S. Petit-Watelot, I. Lucas, L. Morellón, P. A. Algarabel, M. R. Ibarra, R. Miranda, J. Camarero, J. C. Rojas-Sánchez, P. Perna, *APL Mater.* **2021**, *9*, 061113.
[32] S. Lancaster, I. Arnay, R. Guerrero, A. Gudín, A. Guedeja-Marrón, J. M. Diez, J. Gärtner, A. Anadón, M. Varela, J. Camarero, T. Mikolajick, P. Perna, S. Slesazeck, *ACS Appl. Mater. Interfaces* **2023**, *15*, 16963.
[33] T. Nozaki, T. Yamamoto, S. Miwa, M. Tsujikawa, M. Shirai, S. Yuasa, Y. Suzuki, *Micromachines* **2019**, *10*, 327.
[34] P. K. Amiri, K. L. Wang, in *Spin*, vol *2*. World Scientific, Singapore **2012**, p. 1240002.
[35] M. Schott, L. Ranno, H. Béa, C. Baraduc, S. Auffret, A. Bernand-Mantel, *J. Magn. Magn. Mater.* **2021**, *520*, 167122.
[36] T. Srivastava, M. Schott, R. Juge, V. Krizakova, M. Belmeguenai, Y. Roussigné, A. Bernand-Mantel, L. Ranno, S. Pizzini, S.-M. Chérif, A. Stashkevich, S. Auffret, O. Boulle, G. Gaudin, M. Chshiev, C. Baraduc, H. Béa, *Nano Lett.* **2018**, *18*, 4871.
[37] Y. Ba, S. Zhuang, Y. Zhang, Y. Wang, Y. Gao, H. Zhou, M. Chen, W. Sun, Q. Liu, G. Chai, J. Ma, Y. Zhang, H. Tian, H. Du, W. Jiang, C. Nan, J.-M. Hu, Y. Zhao, *Nat. Commun.* **2021**, *12*, 322.
[38] S. Paul, S. Heinze, *npj Comput. Mater.* **2022**, *8*, 105.
[39] P. Huang, M. Cantoni, A. Magrez, F. Carbone, H. M. Rønnow, *Nanoscale* **2022**, *14*, 16655.
[40] C. Ma, X. Zhang, J. Xia, M. Ezawa, W. Jiang, T. Ono, S. Piramanayagam, A. Morisako, Y. Zhou, X. Liu, *Nano Lett.* **2018**, *19*, 353.
[41] Y. Wang, L. Wang, J. Xia, Z. Lai, G. Tian, X. Zhang, Z. Hou, X. Gao, W. Mi, C. Feng, M. Zeng, G. Zhou, G. Yu, G. Wu, Y. Zhou, W. Wang, X.-x. Zhang, J. Liu, *Nat. Commun.* **2020**, *11*, 3577.
[42] F. Ajejas, A. Gudín, R. Guerrero, A. Anadon Barcelona, J. M. Diez, L. de Melo Costa, P. Olleros, M. A. Niño, S. Pizzini, J. Vogel, M. Valvidares,

P. Gargiani, M. Cabero, M. Varela, J. Camarero, R. Miranda, P. Perna, *Nano Lett.* **2018**, *18*, 5364.
[43] F. Ajejas, V. Křižáková, D. de Souza Chaves, J. Vogel, P. Perna, R. Guerrero, A. Gudin, J. Camarero, S. Pizzini, *Appl. Phys. Lett.* **2017**, *111*, 202402.
[44] M. Blanco-Rey, P. Perna, A. Gudin, J. M. Diez, A. Anadón, P. Olleros-Rodríguez, L. de Melo Costa, M. Valvidares, P. Gargiani, A. Guedeja-Marron, M. Cabero, M. Varela, C. García-Fernández, M. M. Otrokov, J. Camarero, R. Miranda, A. Arnau, J. I. Cerdá, *ACS Appl. Nano Mater.* **2021**, *4*, 4398.
[45] P. Olleros-Rodríguez, R. Guerrero, J. Camarero, O. Chubykalo-Fesenko, P. Perna, *ACS Appl. Mater. Interfaces* **2020**, *12*, 25419.
[46] S. Rohart, A. Thiaville, *Phys. Rev. B* **2013**, *88*, 184422.
[47] J. Mulkers, M. V. Milošević, B. Van Waeyenberge, *Phys. Rev. B* **2016**, *93*, 214405.
[48] A. Riveros, F. Tejo, J. Escrig, K. Guslienko, O. Chubykalo-Fesenko, *Phys. Rev. Appl.* **2021**, *16*, 014068.
[49] C. Reichhardt, C. J. O. Reichhardt, M. V. Milošević, *Rev. Mod. Phys.* **2022**, *94*, 035005.
[50] F. Ajejas, Y. Sassi, W. Legrand, T. Srivastava, S. Collin, A. Vecchiola, K. Bouzehouane, N. Reyren, V. Cros, *APL Mater.* **2023**, *11*, 6.
[51] A. Vansteenkiste, J. Leliaert, M. Dvornik, M. Helsen, F. Garcia-Sanchez, B. Van Waeyenberge, *AIP Adv.* **2014**, *4*, 107133.
[52] J. Leliaert, M. Dvornik, J. Mulkers, J. De Clercq, M. Milošević, B. Van Waeyenberge, *J. Phys. D: Appl. Phys.* **2018**, *51*, 123002.
[53] P. Metaxas, J. Jamet, A. Mougin, M. Cormier, J. Ferré, V. Baltz, B. Rodmacq, B. Dieny, R. Stamps, *Phys. Rev. Lett.* **2007**, *99*, 217208.
[54] M. B. Hahn, *J. Phys. Commun.* **2019**, *3*, 075009.
[55] E. Martínez, L. López-Díaz, L. Torres, C. García-Cervera, *J. Phys. D: Appl. Phys.* **2007**, *40*, 942.